NANO LETTERS

pubs.acs.org/NanoLett

Letter

Ultrafast Nanoscopy of High-Density Exciton Phases in WSe_2

Thomas Siday,[▽] Fabian Sandner,[▽] Samuel Brem, Martin Zizlsperger, Raul Perea-Causin, Felix Schiegl, Svenja Nerreter, Markus Plankl, Philipp Merkl, Fabian Mooshammer, Markus A. Huber, Ermin Malic,* and Rupert Huber*

Cite This: *Nano Lett.* 2022, 22, 2561−2568

Read Online

ACCESS | Metrics & More | Article Recommendations | Supporting Information

ABSTRACT: The density-driven transition of an exciton gas into an electron−hole plasma remains a compelling question in condensed matter physics. In two-dimensional transition metal dichalcogenides, strongly bound excitons can undergo this phase change after transient injection of electron−hole pairs. Unfortunately, unavoidable nanoscale inhomogeneity in these materials has impeded quantitative investigation into this elusive transition. Here, we demonstrate how ultrafast polarization nanoscopy can capture the Mott transition through the density-dependent recombination dynamics of electron−hole pairs within a WSe_2 homobilayer. For increasing carrier density, an initial monomolecular recombination of optically dark excitons transitions continuously into a bimolecular recombination of an unbound electron−hole plasma above 7×10^{12} cm^{-2}. We resolve how the Mott transition modulates over nanometer length scales, directly evidencing the strong inhomogeneity in stacked monolayers. Our results demonstrate how ultrafast polarization nanoscopy could unveil the interplay of strong electronic correlations and interlayer coupling within a diverse range of stacked and twisted two-dimensional materials.

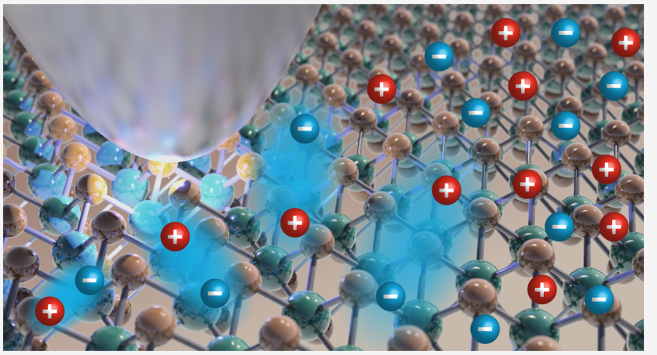

KEYWORDS: *Mott transition, exciton, ultrafast dynamics, near-field microscopy, terahertz, transition metal dichalcogenides*

In semiconductors, Coulomb correlations between electron and hole result in the formation of bound states, known as excitons. The many-body interactions between these quasiparticles at elevated carrier densities are markedly different from those of unbound electron−hole pairs, providing a unique platform for exploring many-body dynamics, as the carrier density can be directly controlled through optical excitation. At high carrier densities, a prototypical Mott transition can emerge, describing the transition from an exciton gas into a plasma of electrons and holes.[1−7] However, the true character of the Mott transition remains controversial. Theoretically, it is challenging to accurately model the Mott transition, as the relative contributions of bound and free carriers to the screening of excitons are difficult to consistently calculate.[4] Experimentally, semiconductor quantum wells have provided a platform to explore the excitonic Mott transition[1,2] but have been constrained by the small exciton binding energy (few millielectronvolts) and conflicting experimental conclusions, with evidence emerging for both continuous and abrupt transitions.[8]

When transition metal dichalcogenides (TMDCs) are thinned to only a few atomic layers, a phase of excitons emerges at room temperature. Their high binding energy, on the order of hundreds of millielectronvolts [ref 9], is a direct result of the reduced dielectric screening and strict quantum confinement to two dimensions. Interlayer coupling is an efficient tuning knob for the dimensionality and environment of excitons and hence provides direct control over the binding energy through stacking and twisting,[10−14] alongside moiré trapping[14−16] and interlayer hybridization.[17−19]

While the excitonic phase in TMDCs is far more stable than that in semiconductor quantum wells, conventional probes of excitons run into several challenges when attempting to characterize the Mott transition. Spatially averaged techniques are prone to inhomogeneous broadening, a result of unavoidable nanoscale inhomogeneity, which emerges during fabrication of all van der Waals (vdW) materials.[20−26] Furthermore, techniques reliant on interband selection rules can easily present a distorted picture of the Mott transition, since only a tiny fraction of excitons, those that obey the selection rules, can contribute to the measured response. This restriction can easily obscure the complex interplay of

Received: December 8, 2021
Revised: February 3, 2022
Published: February 14, 2022

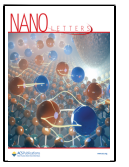

https://doi.org/10.1021/acs.nanolett.1c04741
Nano Lett. 2022, 22, 2561−2568

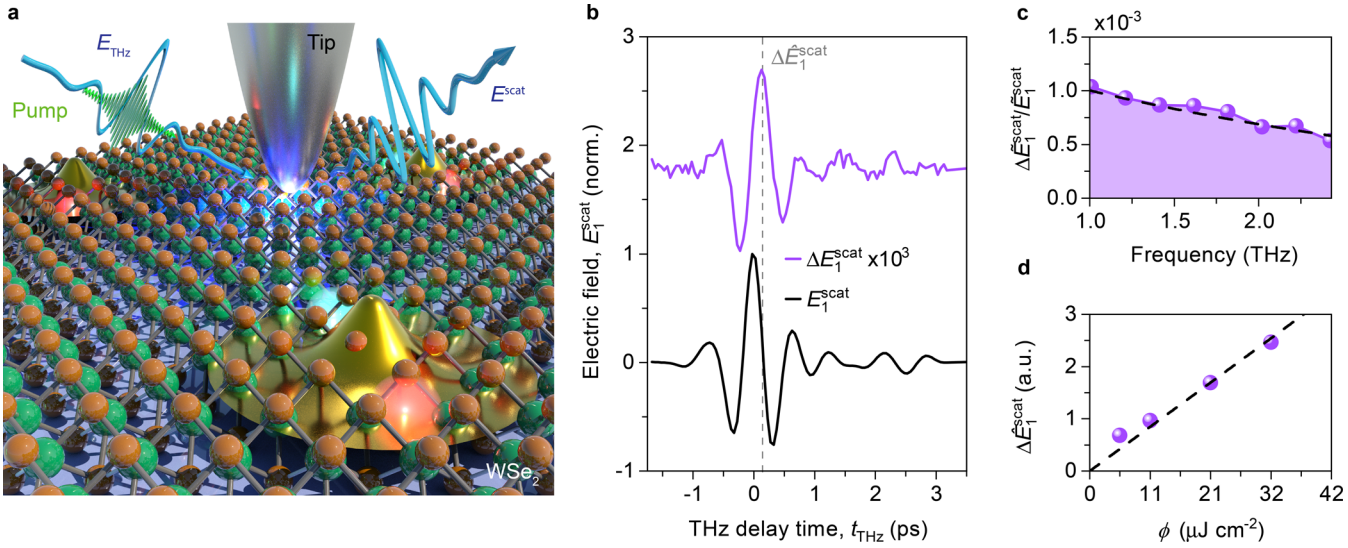

Figure 1. Ultrafast polarization nanoscopy of monolayer WSe_2. (a) Schematic of the terahertz polarization nanoscopy technique. An optical pulse (photon energy 2.4 eV, pulse duration 140 fs) is used for ultrafast interband excitation of electron–hole pairs in a WSe_2 monolayer. Simultaneously, a terahertz probe pulse, coupled to the nanoscale apex of an antenna tip, measures the polarizability of excitons in the monolayer. (b) Steady-state (black line) and pump-induced terahertz waveforms (purple line, offset for clarity) recorded on a monolayer of WSe_2 as a function of the terahertz delay time, t_{THz} (fluence ϕ = 27 μJ cm^{-2}). (c) Relative pump-induced spectral amplitude ($\Delta\tilde{E}_1^{scat}/\tilde{E}_1^{scat}$) for the transients shown in panel b. The dashed line shows the spectral response for a low-frequency Lorentzian oscillator, using a multilayer finite dipole model (see Supporting Information, section 3). (d) Peak of the pump-induced change ($\Delta\hat{E}_1^{scat}$, see dashed gray line in panel b) measured for increasing pump fluence ϕ. The dashed line shows a linear fit to the data.

intervalley scattering,[27−29] Auger recombination,[9,30] and interlayer tunneling within TMDCs.[13,31]

Here, we circumvent these limitations by exploring high-density exciton phases in TMDCs with polarization nanoscopy,[23] a technique based on time-resolved terahertz near-field microscopy.[32−36] This acts as an ultrafast, nanoscale probe of all photoexcited electron–hole pairs, regardless of interband selection rules. We use the technique to observe how increasing the density of hybrid excitons within a twisted bilayer of WSe_2 leads to a gradual Mott transition into a plasma of electrons and holes. These results are fully corroborated with many-body calculations of the excitonic transition.

First, we demonstrate that polarization nanoscopy can deliver quantitative nanoscale insight into the ultrafast dynamics of photoexcited electron–hole pairs in a monolayer of WSe_2. The nanoscopy technique is visualized in Figure 1a. Broadband pulses of terahertz radiation (E_{THz}) are generated through optical rectification and focused onto a platinum–iridium antenna tip mounted as the probe of an atomic force microscope (AFM). A strong near-field interaction between the tip apex and the sample probes the local dielectric function of the TMDC. Here, the spatial resolution achievable with the tip is dictated by the apex radius (20 nm), and results in a spatial resolution of ∼40 nm (ref 23). The terahertz field is then scattered from the tip (E^{scat}) and resolved using electro-optic sampling (Figure 1b, see Supporting Information, section 1 for details). To directly probe the polarizability of photoexcited electron–hole pairs, a transient population of excitons is generated in the monolayer through interband optical excitation (photon energy 2.4 eV, pulse duration 140 fs, s-polarized).

The maximum change to the scattered terahertz pulse, induced by photoexcited electrons and holes (ΔE_1^{scat}) is shown in Figure 1b. The relative spectral amplitude ($\Delta\tilde{E}_1^{scat}/\tilde{E}_1^{scat}$) of the pump-induced change can then be extracted from the scattered transients through Fourier analysis, as shown in Figure 1c. The signal is dominated by a monotonic slope, decaying at high frequencies. Microscopically, this broad spectral response can originate from several sources: first, quantum transitions of excitons in WSe_2 dominate the mid-infrared frequency range,[9,37] with transitions between excited exciton states extending across the terahertz spectrum.[13,38] These transitions, alongside contributions from quasi-free carriers[38] shape the in-plane spectral response of the monolayer. While the out-of-plane polarizability of the monolayer is significantly weaker than in-plane, the strong out-of-plane field sensitivity of the tip means that contributions in- and out-of-plane combine[23,39] to form the monotonic spectral response seen in Figure 1c (Supporting Information, section 2). We can accurately model this spectrum by applying a low-frequency Lorentz oscillator to a multilayer finite dipole model[40] (Supporting Information, section 3). In Figure 1d, we see that the peak of the pump-induced change, $\Delta\hat{E}_1^{scat}$ (vertical dashed line in Figure 1b) scales linearly with increasing optical pump fluence. This can be expected, as previous studies have demonstrated that unless a dramatic change in polarizability occurs (for example, interlayer tunneling of photoexcited electron–hole pairs), ultrafast nanoscopy places similar weight over all photoexcited charge carriers, regardless of interband selection rules.[23] This demonstrates the strength of the technique for quantitative measurement of quasiparticle density in TMDCs.

We now test if ultrafast polarization nanoscopy can be used to identify the presence of excitons through their recombination dynamics in the monolayer. Spatially averaged measurements have revealed that the picosecond recombination in monolayer WSe_2 at high carrier densities is a bimolecular (two particle[41]) process. Microscopically, this recombination emerges in response to Auger annihilation of excitons.[9,42] We gain insight into these dynamics by measuring the peak of

https://doi.org/10.1021/acs.nanolett.1c04741
Nano Lett. 2022, 22, 2561−2568

the pump-induced change, $\Delta\hat{E}_1^{scat}$, as a function of pump delay time, t_p. This pump−probe measurement is shown in Figure 2

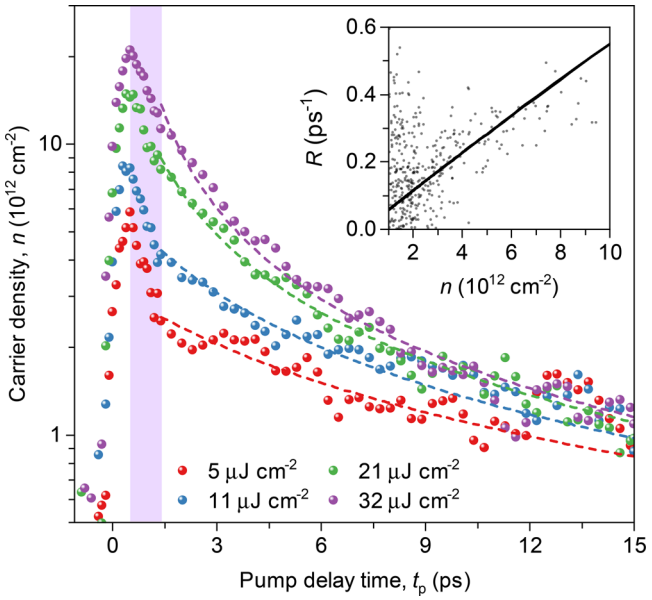

Figure 2. Pump-induced terahertz near-field response of monolayer WSe_2 at high carrier densities. Carrier density in monolayer WSe_2 measured as a function of pump delay time, t_p (spheres), for increasing pump fluence, extracted from the peak of the pump-induced change $\Delta\hat{E}_1^{scat}$ (see main text and Supporting Information, section 4). The recombination coefficient R (inset, black line) can then be extracted by fitting a bimolecular rate equation for $t_p > 1.5$ ps (dashed lines). We also extract R directly from the experimental data (gray points). See Supporting Information, sections 5 and 6, for further details.

as the fluence of the optical pump pulse is scaled from 5 to 32 μJ cm^{-2}, which we convert to carrier density considering the optical absorption of the monolayer and using a finite-difference time-domain solver to account for the oblique incidence angle of the optical pump beam (Supporting Information, section 4).

Following the peak of the pump−probe response, a rapid (~1 ps) decay occurs, agreeing well with the time scale for exciton formation in TMDC monolayers.[27,28,38] After this formation time ($t_p > 1.5$ ps), the pump−probe response can be accurately modeled by fitting a bimolecular rate equation to all curves (Figure 2, dashed lines), where the extracted decay constant, $\Gamma = 0.06$ cm^2 s^{-1}, agrees well with spatially averaged measurements[9] (see Supporting Information, section 5, for details of the fitting procedure). To provide an intuitive picture of the density-dependent recombination dynamics of the monolayer, we plot the recombination coefficient, R (see Supporting Information, section 6) for $t_p > 1.5$ ps as a function of carrier density (Figure 2, inset). For a monomolecular (single particle) decay, R will remain constant at all densities, whereas a bimolecular decay process will appear as a linear slope in R as the carrier density increases. For delay times $t_p > 1.5$ ps, the recombination coefficient extracted from the rate equation model increases linearly with density (solid line). We confirm the bimolecular nature of the recombination process by plotting R extracted directly from the experimental data (gray dots). The good agreement between our near-field and previous far-field measurements indicates that excitonic Auger annihilation dominates the recombination processes in the monolayer for our experiments. Intriguingly, at elevated carrier density, the rapid initial decay at times $t_p < 1.5$ ps begins to merge with the Auger recombination rate, hinting at an incipient phase transition in the monolayer.

While inhomogeneity is present in all vdW materials, we can still attain qualitative agreement with spatially averaged measurements on the monolayer. Conversely, quantitative measurement of high density many-body physics in TMDCs can be entirely obscured to spatially averaged probes, as nanoscale disorder leads to inhomogeneous broadening. We now show that ultrafast polarization nanoscopy can directly access the Mott transition in stacked and twisted TMDCs and quantitatively resolve how nanoscale disorder within the bilayer can tune the behavior of the transition.

Estimates for the Mott transition in WSe_2 monolayers require carrier densities on the order of 10^{13}−10^{14} cm^{-2} [refs 3 and 4], which, for the high repetition rate of our laser system needed for near-field microscopy, lies above the material's damage threshold. Alternatively, when two WSe_2 monolayers are stacked, interlayer coupling suppresses the binding energy of the exciton,[43] with further control through altering the relative twist angle between monolayers.[17] We exploit this degree of freedom by preparing a homobilayer of WSe_2 with a 0° twist angle (equivalent to 3R stacking), using mechanical exfoliation and all-dry viscoelastic stamping (Supporting Information, section 7). In this configuration, the exciton binding energy is minimized,[17] promising access to the Mott transition at much reduced pump fluences and avoiding sample degradation.

We now trace the ultrafast pump−probe response of the homobilayer (Figure 3a), while increasing the fluence of the optical pump from 3 to 27 μJ cm^{-2}. In all cases, the response is markedly different from that of the monolayer. Most importantly, we see a dramatic increase in the decay time, from a few picoseconds to hundreds of picoseconds in the homobilayer. This increased lifetime is a direct result of the predominantly momentum-indirect recombination[44] in bilayer WSe_2, which is further corroborated by the distinct lack of any rapid recombination at early pump−probe times, in contrast to the monolayer (Figure 2).

On closer inspection, further discrepancies emerge. At low optical pump fluence (3 and 5 μJ cm^{-2}), recombination in the homobilayer appears linear on the logarithmic density scale of Figure 3a. This indicates a monomolecular (single particle) recombination process, characteristic of noninteracting dark excitons.[41] This process is depicted on the right-hand side of Figure 3a. Intriguingly, for fluences above 5 μJ cm^{-2}, the recombination dynamics become nonlinear and can be well reproduced by adding a two particle recombination process. To this end, we fit the density-dependent dynamics of all pump−probe curves with a bipartite rate equation, describing the transition from monomolecular to bimolecular (two particle) recombination as the density of electron−hole pairs is increased:

$$\frac{dn}{dt} = -f(n - n_c)\Gamma_b n^2 - [1 - f(n - n_c)]\Gamma_m n \quad (1)$$

Here, n is the electron−hole pair density, and Γ_m and Γ_b represent monomolecular and bimolecular recombination constants, respectively. We separate the mono- and bimolecular decay regimes in density with the function $f(n - n_c) = \theta(n - n_c) \times G(n - n_c)$, the convolution of a Heaviside function $\theta(n - n_c)$ with a Gaussian $G(n - n_c)$. This allows us to

https://doi.org/10.1021/acs.nanolett.1c04741
Nano Lett. 2022, 22, 2561−2568

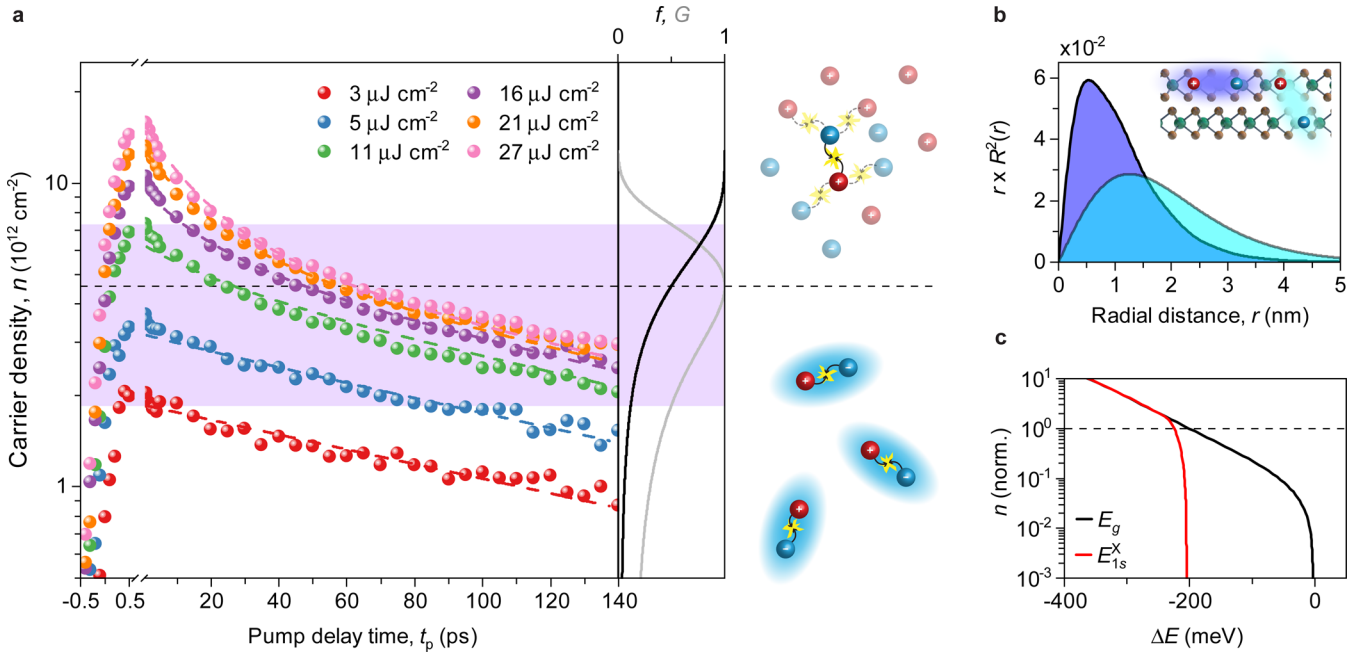

Figure 3. Excitonic Mott transition in a twisted bilayer of WSe_2. (a) Carrier density in the homobilayer measured as a function of pump delay time, t_p, for increasing pump fluence (spheres), extracted from the peak of the pump-induced change $\Delta\hat{E}_1^{scat}$ (see main text). The dashed lines are fitted to all pump−probe curves simultaneously using eq 1. The shaded area represents the width (Δn) of the transition function f, and the black dashed line illustrates the center of the transition, n_c. The center panel shows the transition function, f (black), together with the corresponding Gaussian, G (gray). On the right-hand side, monomolecular recombination of excitons is illustrated (bottom), where a Coulomb-bound electron recombines with its hole companion. In the bimolecular electron−hole plasma phase (top), each electron and hole have many potential partners for recombination. (b) Computed radial probability distribution for intra- and interlayer excitonic species (blue and cyan curves, respectively). The inset is a visualization of the two exciton species. (c) Density-dependent renormalization of the bandgap, E_g (black), and the energy of the 1s A-exciton, E_{1s}^X (red), calculated in the framework of the generalized Wannier equation. The dashed horizontal line marks the density at which the exciton gas transitions entirely into an electron−hole plasma.

parametrize the transition with a center n_c and a full-width at half-maximum Δn. After fitting this rate equation to the data in Figure 3a, we extract $n_c = 4.6 \times 10^{12}$ cm^{-2} and $\Delta n = 5.5 \times 10^{12}$ cm^{-2} for the homobilayer.

We attribute the microscopic origin of the bimolecular term in the homobilayer to the recombination of unbound electron−hole pairs,[41] depicted on the right-hand side of Figure 3a. Here, in contrast to the monolayer, Auger recombination is suppressed since excitons are indirect and hybridize between the constituent layers.[12,17] For densities higher than $n_c + \frac{\Delta n}{2} = 7.4 \times 10^{12}$ cm^{-2}, there is an almost complete transition (see Figure 3a, center panel) to bimolecular recombination of electron−hole pairs.

We now show that the most likely candidate for this transition in the homobilayer is a Mott transition, which we quantify through density matrix theory using material parameters from density functional theory. The density at which a gas of excitons dissociates into a weakly bound plasma of electrons and holes is provided by the Mott criterion:[45] $n_c = \left(\frac{0.25}{a_B}\right)^2$, where a_B is the exciton Bohr radius. To calculate an effective in-plane Bohr radius for twisted bilayer WSe_2, we consider the most energetically favorable exciton species in bilayer WSe_2, K−Λ excitons. The Λ and Λ′ valleys consist of selenium p-orbitals, the wave functions of which overlap with the adjacent monolayer. This leads to efficient interlayer hopping of electrons and hybridization of intra- and interlayer excitonic species, especially for 3R stacking.[17] By computing the Bohr radii and relative contribution of intralayer and interlayer exciton species (0.53 nm, 55%, and 1.27 nm, 45%, respectively, see Figure 3b), we determine an effective Bohr radius for the hybrid exciton, $a_B = 0.86$ nm (see Supporting Information, section 8, for details). Using the Mott criterion above, this corresponds to a transition density of 8.5×10^{12} cm^{-2}. This critical density is in extremely good agreement with the rate equation model, where the density at which unbound electron−hole pairs dominate recombination is 7.4×10^{12} cm^{-2}.

To further understand the nature of the Mott transition, we compute the excitonic eigenstates at elevated densities within the framework of the generalized Wannier equation,[46] which accounts for the bandgap renormalization and reduction of binding energy due to Pauli blocking and Lindhard screening. Figure 3c shows the renormalization of bandgap, E_g and the 1s A-exciton energy, E_{1s}^X as a function of increasing density of electrons and holes. At low electron−hole pair density, little to no renormalization of the exciton binding energy (defined as $E_b = E_g - E_{1s}^X$) or bandgap occurs. As the density increases, both are suppressed in response to elevated electronic screening, until the exciton binding energy drops below $\sim k_B T$ (dashed line in Figure 3c), where excitons thermalize into an electron−hole plasma. The qualitative behavior of our model agrees well with prior theoretical studies,[4] reproducing the cancellation of exciton binding energy and bandgap renormalization. We note that quantitatively the threshold for the Mott transition is underestimated, since the Lindhard screening utilized in this model does not account for the reduced polarizability of bound charge carriers compared to

https://doi.org/10.1021/acs.nanolett.1c04741
Nano Lett. 2022, 22, 2561−2568

free particles. A detailed description of the model is provided in Supporting Information, section 9.

The qualitative behavior of the model is succinctly replicated in our experimental findings, which becomes clear by evaluating the recombination coefficient, R, for the homobilayer, which we extract for three representative locations in Figure 4a. For each position of the near-field probe, at low

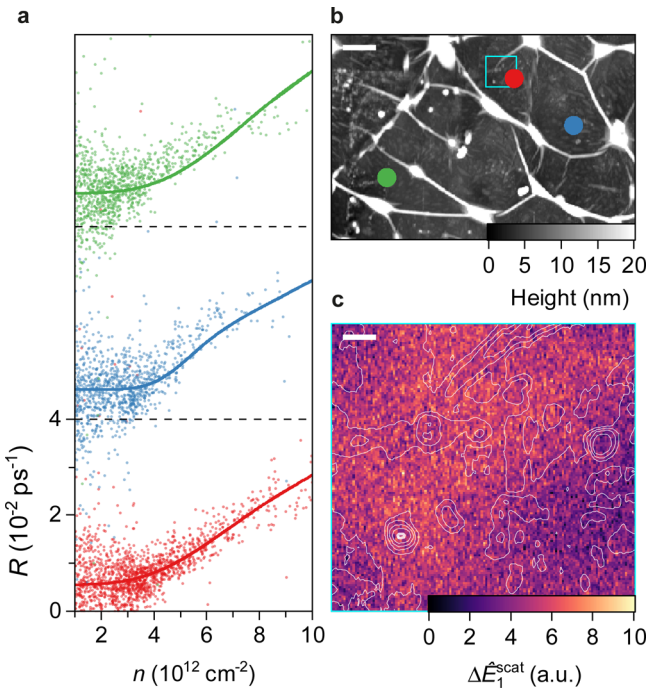

Figure 4. Nanoscale modulation of the exciton Mott transition. (a) Fitted (solid line) and numerically extracted (points) recombination coefficient R (similar to Figure 2, inset), retrieved from fluence-dependent pump−probe measurements (see Supporting Information, section 10) on the homobilayer on three representative locations. While the qualitative trend of R remains similar (unchanging at low densities and increasing linearly for higher densities), sample inhomogeneities lead to quantitative changes. (b) Topography map acquired with AFM showing the three locations where R is extracted. Scale bar: 1 μm. (c) Amplitude of the pump-induced change, $\Delta\hat{E}_1^{\mathrm{scat}}$, at the peak of the pump−probe response, in the region indicated by the cyan square in panel b. The modulation of $\Delta\hat{E}_1^{\mathrm{scat}}$ indicates that the inhomogeneity of the Mott transition observed in panel a continues to the nanoscale. The white isolines show the corresponding AFM topography. Scale bar: 100 nm.

carrier densities, R is constant and independent of carrier density (monomolecular), as predicted by the model in Figure 3c. As we reach the critical density for the Mott transition, there is a gradual upturn in R, which ultimately becomes linear at high carrier density, indicative of bimolecular recombination. This gradual transition coincides with the renormalization process predicted in Figure 3c. Critically, the recombination coefficient shows that this Mott transition from an exciton gas to an electron−hole plasma is continuous even on the nanoscale, where the presence of inhomogeneous broadening is almost entirely eliminated.

We therefore propose a simplified microscopic picture of this continuous Mott transition, considering both our theoretical and experimental results (Figures 3c and 4a). At low carrier density, excitons recombine nonradiatively in the homobilayer, where Auger recombination is suppressed in response to the indirect and interlayer nature of the hybrid exciton.[12,17] As the carrier density increases, excitonic and electronic screening drive renormalization of the exciton binding energy. This, alongside the gradual increase in relative density of quasi-unbound electron−hole pairs, results in an increase of the recombination coefficient in the experiment.[41] As the pair density continues to increase, the exciton binding energy is renormalized so strongly that electrons and holes effectively dissociate into a weakly bound plasma-like phase, demonstrated by the linearly increasing recombination coefficient at the highest carrier densities. This Mott transition is the most likely candidate for the density-dependent dynamics of the homobilayer, with processes of this kind predicted[8] and measured[3,4] with spatially averaged techniques.

While the recombination coefficient displays the same qualitative behavior in all three measurement positions on the homobilayer, the critical density, transition width, and instantaneous decay constants all vary between locations. This indicates that inhomogeneity in the homobilayer can modify the properties of excitons and unbound electron−hole pairs on the nanoscale. Intriguingly, this modulation of R occurs within comparable regions of the homobilayer that appear topographically homogeneous in the AFM image (Figure 4b). The microscopic origin of these changes can emerge either from inclusion of dielectric adsorbates to the surface of the homobilayer,[20] which modifies the local dielectric environment, or in response to nanoscale variation in the local twist angle and strain, both of which[17,47] have been demonstrated to modify the exciton binding energy. Finally, nanoscale fluctuations in the density of atomic defects could also substantially alter the dynamics of the Mott transition, for example by trapping itinerant excitons within chalcogen vacancies,[48] which could suppress the critical density and modify recombination processes. As these changes are partially reflected by modulations in the magnitude of the peak pump-induced change, $\Delta\hat{E}_1^{\mathrm{scat}}$, we can resolve these nanoscale changes (Figure 4c) by imaging a region of the homobilayer. A clear modulation in the amplitude of $\Delta\hat{E}_1^{\mathrm{scat}}$ within this region is visible, which does not correlate strongly with topographic features (white isolines). Crucially, this indicates that the exciton binding energy can be modulated over length scales inaccessible to any other noncontact ultrafast nanoscopy technique, demonstrating that ultrafast polarization nanoscopy is indispensable for the study of intrinsically disordered vdW materials.

In summary, we have probed the ultrafast nonequilibrium dynamics of excitons in TMDC monolayers and homobilayers with nanoscale spatial resolution. In the monolayer, our findings agree well with spatially averaged techniques, proving the potential for ultrafast polarization nanoscopy as a subcycle probe of excitons on the nanoscale. In twisted bilayer WSe_2, we see that as the density of carriers is increased, the exciton phase smoothly transitions into a weakly bound plasma of electrons and holes. The unavoidable inhomogeneity present in all vdW materials results in nanoscale modulation of this excitonic Mott transition. In the future, ultrafast nanoscopy could compare systems of different dimensionality; for example, many-body dynamics of electrons and holes in one-dimensional materials, where excitons can avoid dissociation even at the highest pump fluences.[49] Furthermore, it will be particularly interesting to understand how excitons at low temperatures may couple to a variety of quantum phases of

https://doi.org/10.1021/acs.nanolett.1c04741
Nano Lett. 2022, 22, 2561−2568

matter, including electronic crystallization,[50] condensation,[51] or magnetic order.[52]

■ ASSOCIATED CONTENT

Supporting Information

The Supporting Information is available free of charge at https://pubs.acs.org/doi/10.1021/acs.nanolett.1c04741.

Experimental setup, sensitivity to the in-plane and out-of-plane spectral response of monolayer WSe_2, multilayer scattering model, carrier density calculation, rate equation fitting, recombination coefficient R, sample fabrication, calculation of effective Bohr radius, density-dependent renormalization of the exciton binding energy, fluence-dependent pump−probe measurements, and peak pump-induced change for increasing fluence on the WSe_2 homobilayer (PDF)

■ AUTHOR INFORMATION

Corresponding Authors

Ermin Malic − *Department of Physics, Philipps-Universität Marburg, 35032 Marburg, Germany; Department of Physics, Chalmers University of Technology, 41296 Gothenburg, Sweden*; Email: ermin.malic@physik.uni-marburg.de

Rupert Huber − *Department of Physics and Regensburg Center for Ultrafast Nanoscopy (RUN), University of Regensburg, 93040 Regensburg, Germany*; Email: rupert.huber@physik.uni-regensburg.de

Authors

Thomas Siday − *Department of Physics and Regensburg Center for Ultrafast Nanoscopy (RUN), University of Regensburg, 93040 Regensburg, Germany*; orcid.org/0000-0003-0157-3233

Fabian Sandner − *Department of Physics and Regensburg Center for Ultrafast Nanoscopy (RUN), University of Regensburg, 93040 Regensburg, Germany*

Samuel Brem − *Department of Physics, Philipps-Universität Marburg, 35032 Marburg, Germany; Department of Physics, Chalmers University of Technology, 41296 Gothenburg, Sweden*

Martin Zizlsperger − *Department of Physics and Regensburg Center for Ultrafast Nanoscopy (RUN), University of Regensburg, 93040 Regensburg, Germany*

Raul Perea-Causin − *Department of Physics, Chalmers University of Technology, 41296 Gothenburg, Sweden*

Felix Schiegl − *Department of Physics and Regensburg Center for Ultrafast Nanoscopy (RUN), University of Regensburg, 93040 Regensburg, Germany*

Svenja Nerreter − *Department of Physics and Regensburg Center for Ultrafast Nanoscopy (RUN), University of Regensburg, 93040 Regensburg, Germany*

Markus Plankl − *Department of Physics and Regensburg Center for Ultrafast Nanoscopy (RUN), University of Regensburg, 93040 Regensburg, Germany*

Philipp Merkl − *Department of Physics and Regensburg Center for Ultrafast Nanoscopy (RUN), University of Regensburg, 93040 Regensburg, Germany*

Fabian Mooshammer − *Department of Physics and Regensburg Center for Ultrafast Nanoscopy (RUN), University of Regensburg, 93040 Regensburg, Germany; Department of Physics, Columbia University, New York, New York 10027, United States*; orcid.org/0000-0002-9744-2694

Markus A. Huber − *Department of Physics and Regensburg Center for Ultrafast Nanoscopy (RUN), University of Regensburg, 93040 Regensburg, Germany*

Complete contact information is available at: https://pubs.acs.org/10.1021/acs.nanolett.1c04741

Author Contributions

[▽]T. Siday and F. Sandner contributed equally. T. Siday, F. Sandner., M. Zizlsperger, F. Schiegl, S. Nerreter, M. Plankl, P. Merkl, F. Mooshammer, M. A. Huber, and R. Huber performed the experiments and analyzed the data. F. Mooshammer fabricated the samples. S. Brem, R. Perea-Causin, and E. Malic computed exciton wave functions and density-dependent renormalization. T. Siday and M. A. Huber calculated the multilayer scattering model. T. Siday, M. Zizlsperger, and M. A. Huber fitted the rate equation model. All authors contributed to the discussions of the results. The manuscript was written by T. Siday, F. Sandner, S. Brem, R. Perea-Causin, M. A. Huber, E. Malic, and R. Huber with input from all authors.

Notes

The authors declare no competing financial interest.

■ ACKNOWLEDGMENTS

We thank M. Furthmeier for technical assistance. This work was supported by the Deutsche Forschungsgemeinschaft (DFG, German Research Foundation), Project-ID 314695032, SFB 1277 (Project A05), and SFB 1083 (Project B9), and through research grant HU1598/8. The work was also supported by the European Union's Horizon 2020 research and innovation program under grant agreement no. 881603 (Graphene Flagship). F. Mooshammer gratefully acknowledges support by the Alexander von Humboldt Foundation.

■ REFERENCES

(1) Kappei, L.; Szczytko, J.; Morier-Genoud, F.; Deveaud, B. Direct Observation of the Mott Transition in an Optically Excited Semiconductor Quantum Well. *Phys. Rev. Lett.* **2005**, *94* (14), 147403.

(2) Stern, M.; Garmider, V.; Umansky, V.; Bar-Joseph, I. Mott Transition of Excitons in Coupled Quantum Wells. *Phys. Rev. Lett.* **2008**, *100* (25), 256402.

(3) Chernikov, A.; Ruppert, C.; Hill, H. M.; Rigosi, A. F.; Heinz, T. F. Population Inversion and Giant Bandgap Renormalization in Atomically Thin WS_2 Layers. *Nat. Photonics* **2015**, *9* (7), 466−470.

(4) Steinhoff, A.; Florian, M.; Rösner, M.; Schönhoff, G.; Wehling, T. O.; Jahnke, F. Exciton Fission in Monolayer Transition Metal Dichalcogenide Semiconductors. *Nat. Commun.* **2017**, *8* (1), 1166.

(5) Bataller, A. W.; Younts, R. A.; Rustagi, A.; Yu, Y.; Ardekani, H.; Kemper, A.; Cao, L.; Gundogdu, K. Dense Electron-Hole Plasma Formation and Ultralong Charge Lifetime in Monolayer MoS_2 via Material Tuning. *Nano Lett.* **2019**, *19* (2), 1104−1111.

(6) Wang, J.; Ardelean, J.; Bai, Y.; Steinhoff, A.; Florian, M.; Jahnke, F.; Xu, X.; Kira, M.; Hone, J.; Zhu, X.-Y. Optical Generation of High Carrier Densities in 2D Semiconductor Heterobilayers. *Sci. Adv.* **2019**, *5* (9), eaax0145.

(7) Wang, J.; Shi, Q.; Shih, E.-M.; Zhou, L.; Wu, W.; Bai, Y.; Rhodes, D.; Barmak, K.; Hone, J.; Dean, C. R.; Zhu, X.-Y. Diffusivity Reveals Three Distinct Phases of Interlayer Excitons in $MoSe_2/WSe_2$ Heterobilayers. *Phys. Rev. Lett.* **2021**, *126* (10), 106804.

(8) Guerci, D.; Capone, M.; Fabrizio, M. Exciton Mott Transition Revisited. *Phys. Rev. Materials* **2019**, *3* (5), 054605.
(9) Poellmann, C.; Steinleitner, P.; Leierseder, U.; Nagler, P.; Plechinger, G.; Porer, M.; Bratschitsch, R.; Schüller, C.; Korn, T.; Huber, R. Resonant Internal Quantum Transitions and Femtosecond Radiative Decay of Excitons in Monolayer WSe_2. *Nat. Mater.* **2015**, *14* (9), 889−893.
(10) Geim, A. K.; Grigorieva, I. V. van der Waals Heterostructures. *Nature* **2013**, *499*, 419−425.
(11) Lee, C.-H.; Lee, G.-H.; van der Zande, A. M.; Chen, W.; Li, Y.; Han, M.; Cui, X.; Arefe, G.; Nuckolls, C.; Heinz, T. F.; Guo, J.; Hone, J.; Kim, P. Atomically Thin p-n Junctions with van der Waals Heterointerfaces. *Nat. Nanotechnol.* **2014**, *9* (9), 676−681.
(12) Rivera, P.; Yu, H.; Seyler, K. L.; Wilson, N. P.; Yao, W.; Xu, X. Interlayer Valley Excitons in Heterobilayers of Transition Metal Dichalcogenides. *Nat. Nanotechnol.* **2018**, *13* (11), 1004−1015.
(13) Merkl, P.; Mooshammer, F.; Steinleitner, P.; Girnghuber, A.; Lin, K.-Q.; Nagler, P.; Holler, J.; Schüller, C.; Lupton, J. M.; Korn, T.; Ovesen, S.; Brem, S.; Malic, E.; Huber, R. Ultrafast Transition between Exciton Phases in van der Waals Heterostructures. *Nat. Mater.* **2019**, *18* (7), 691−696.
(14) Brem, S.; Linderälv, C.; Erhart, P.; Malic, E. Tunable Phases of Moiré Excitons in van der Waals Heterostructures. *Nano Lett.* **2020**, *20* (12), 8534−8540.
(15) Seyler, K. L.; Rivera, P.; Yu, H.; Wilson, N. P.; Ray, E. L.; Mandrus, D. G.; Yan, J.; Yao, W.; Xu, X. Signatures of Moiré-Trapped Valley Excitons in $MoSe_2/WSe_2$ Heterobilayers. *Nature* **2019**, *567* (7746), 66−70.
(16) Tran, K.; Moody, G.; Wu, F.; Lu, X.; Choi, J.; Kim, K.; Rai, A.; Sanchez, D. A.; Quan, J.; Singh, A.; Embley, J.; Zepeda, A.; Campbell, M.; Autry, T.; Taniguchi, T.; Watanabe, K.; Lu, N.; Banerjee, S. K.; Silverman, K. L.; Kim, S.; Tutuc, E.; Yang, L.; MacDonald, A. H.; Li, X. Evidence for Moiré Excitons in van der Waals Heterostructures. *Nature* **2019**, *567* (7746), 71−75.
(17) Merkl, P.; Mooshammer, F.; Brem, S.; Girnghuber, A.; Lin, K.-Q.; Weigl, L.; Liebich, M.; Yong, C.-K.; Gillen, R.; Maultzsch, J.; Lupton, J. M.; Malic, E.; Huber, R. Twist-Tailoring Coulomb Correlations in van der Waals Homobilayers. *Nat. Commun.* **2020**, *11* (1), 2167.
(18) Kunstmann, J.; Mooshammer, F.; Nagler, P.; Chaves, A.; Stein, F.; Paradiso, N.; Plechinger, G.; Strunk, C.; Schüller, C.; Seifert, G.; Reichman, D. R.; Korn, T. Momentum-Space Indirect Interlayer Excitons in Transition-Metal Dichalcogenide van der Waals Heterostructures. *Nat. Phys.* **2018**, *14* (8), 801−805.
(19) Brem, S.; Lin, K.-Q.; Gillen, R.; Bauer, J. M.; Maultzsch, J.; Lupton, J. M.; Malic, E. Hybridized Intervalley Moiré Excitons and Flat Bands in Twisted WSe_2 Bilayers. *Nanoscale* **2020**, *12* (20), 11088−11094.
(20) Raja, A.; Waldecker, L.; Zipfel, J.; Cho, Y.; Brem, S.; Ziegler, J. D.; Kulig, M.; Taniguchi, T.; Watanabe, K.; Malic, E.; Heinz, T. F.; Berkelbach, T. C.; Chernikov, A. Dielectric Disorder in Two-Dimensional Materials. *Nat. Nanotechnol.* **2019**, *14* (9), 832−837.
(21) McGilly, L. J.; Kerelsky, A.; Finney, N. R.; Shapovalov, K.; Shih, E.-M.; Ghiotto, A.; Zeng, Y.; Moore, S. L.; Wu, W.; Bai, Y.; Watanabe, K.; Taniguchi, T.; Stengel, M.; Zhou, L.; Hone, J.; Zhu, X.; Basov, D. N.; Dean, C.; Dreyer, C. E.; Pasupathy, A. N. Visualization of Moiré Superlattices. *Nat. Nanotechnol.* **2020**, *15* (7), 580−584.
(22) Uri, A.; Grover, S.; Cao, Y.; Crosse, J. A.; Bagani, K.; Rodan-Legrain, D.; Myasoedov, Y.; Watanabe, K.; Taniguchi, T.; Moon, P.; Koshino, M.; Jarillo-Herrero, P.; Zeldov, E. Mapping the Twist-Angle Disorder and Landau Levels in Magic-Angle Graphene. *Nature* **2020**, *581* (7806), 47−52.
(23) Plankl, M.; Faria Junior, P. E.; Mooshammer, F.; Siday, T.; Zizlsperger, M.; Sandner, F.; Schiegl, F.; Maier, S.; Huber, M. A.; Gmitra, M.; Fabian, J.; Boland, J. L.; Cocker, T. L.; Huber, R. Subcycle Contact-Free Nanoscopy of Ultrafast Interlayer Transport in Atomically Thin Heterostructures. *Nat. Photonics* **2021**, *15* (8), 594−600.
(24) Hesp, N. C. H.; Torre, I.; Barcons-Ruiz, D.; Herzig Sheinfux, H.; Watanabe, K.; Taniguchi, T.; Krishna Kumar, R.; Koppens, F. H. L. Nano-Imaging Photoresponse in a Moiré Unit Cell of Minimally Twisted Bilayer Graphene. *Nat. Commun.* **2021**, *12* (1), 1640.
(25) de Jong, T. A.; Benschop, T.; Chen, X.; Krasovskii, E. E.; de Dood, M. J. A.; Tromp, R. M.; Allan, M. P.; van der Molen, S. J. Imaging Moiré Deformation and Dynamics in Twisted Bilayer Graphene. *Nat. Commun.* **2022**, *13*, 70.
(26) Halbertal, D.; Finney, N. R.; Sunku, S. S.; Kerelsky, A.; Rubio-Verdú, C.; Shabani, S.; Xian, L.; Carr, S.; Chen, S.; Zhang, C.; Wang, L.; Gonzalez-Acevedo, D.; McLeod, A. S.; Rhodes, D.; Watanabe, K.; Taniguchi, T.; Kaxiras, E.; Dean, C. R.; Hone, J. C.; Pasupathy, A. N.; Kennes, D. M.; Rubio, A.; Basov, D. N. Moiré Metrology of Energy Landscapes in van der Waals Heterostructures. *Nat. Commun.* **2021**, *12* (1), 242.
(27) Madéo, J.; Man, M. K. L.; Sahoo, C.; Campbell, M.; Pareek, V.; Wong, E. L.; Al-Mahboob, A.; Chan, N. S.; Karmakar, A.; Mariserla, B. M. K.; Li, X.; Heinz, T. F.; Cao, T.; Dani, K. M. Directly Visualizing the Momentum-Forbidden Dark Excitons and Their Dynamics in Atomically Thin Semiconductors. *Science* **2020**, *370* (6521), 1199−1204.
(28) Wallauer, R.; Perea-Causin, R.; Münster, L.; Zajusch, S.; Brem, S.; Güdde, J.; Tanimura, K.; Lin, K.-Q.; Huber, R.; Malic, E.; Höfer, U. Momentum-Resolved Observation of Exciton Formation Dynamics in Monolayer WS_2. *Nano Lett.* **2021**, *21* (13), 5867−5873.
(29) Selig, M.; Berghäuser, G.; Richter, M.; Bratschitsch, R.; Knorr, A.; Malic, E. Dark and Bright Exciton Formation, Thermalization, and Photoluminescence in Monolayer Transition Metal Dichalcogenides. *2D Mater.* **2018**, *5* (3), 035017.
(30) Erkensten, D.; Brem, S.; Wagner, K.; Gillen, R.; Perea-Causin, R.; Ziegler, J. D.; Taniguchi, T.; Watanabe, K.; Maultzsch, J.; Chernikov, A.; Malic, E. Dark exciton-exciton annihilation in monolayer WSe_2. *Phys. Rev. B* **2021**, *104*, L241406.
(31) Ma, E. Y.; Guzelturk, B.; Li, G.; Cao, L.; Shen, Z.-X.; Lindenberg, A. M.; Heinz, T. F. Recording Interfacial Currents on the Subnanometer Length and Femtosecond Time Scale by Terahertz Emission. *Science Advances* **2019**, *5* (2), eaau0073.
(32) Moon, K.; Do, Y.; Lim, M.; Lee, G.; Kang, H.; Park, K. S.; Han, H. Quantitative Coherent Scattering Spectra in Apertureless Terahertz Pulse Near-Field Microscopes. *Appl. Phys. Lett.* **2012**, *101* (1), 011109.
(33) Siday, T.; Hale, L. L.; Hermans, R. I.; Mitrofanov, O. Resonance-Enhanced Terahertz Nanoscopy Probes. *ACS Photonics* **2020**, *7* (3), 596−601.
(34) Zhang, J.; Chen, X.; Mills, S.; Ciavatti, T.; Yao, Z.; Mescall, R.; Hu, H.; Semenenko, V.; Fei, Z.; Li, H.; Perebeinos, V.; Tao, H.; Dai, Q.; Du, X.; Liu, M. Terahertz Nanoimaging of Graphene. *ACS Photonics* **2018**, *5* (7), 2645−2651.
(35) Kim, R. H. J.; Huang, C.; Luan, Y.; Wang, L.-L.; Liu, Z.; Park, J.-M.; Luo, L.; Lozano, P. M.; Gu, G.; Turan, D.; Yardimci, N. T.; Jarrahi, M.; Perakis, I. E.; Fei, Z.; Li, Q.; Wang, J. Terahertz Nano-Imaging of Electronic Strip Heterogeneity in a Dirac Semimetal. *ACS Photonics* **2021**, *8* (7), 1873−1880.
(36) Pizzuto, A.; Castro-Camus, E.; Wilson, W.; Choi, W.; Li, X.; Mittleman, D. M. Nonlocal Time-Resolved Terahertz Spectroscopy in the Near Field. *ACS Photonics* **2021**, *8*, 2904.
(37) Sternbach, A. J.; Chae, S. H.; Latini, S.; Rikhter, A. A.; Shao, Y.; Li, B.; Rhodes, D.; Kim, B.; Schuck, P. J.; Xu, X.; Zhu, X.-Y.; Averitt, R. D.; Hone, J.; Fogler, M. M.; Rubio, A.; Basov, D. N. Programmable Hyperbolic Polaritons in van der Waals Semiconductors. *Science* **2021**, *371* (6529), 617−620.
(38) Steinleitner, P.; Merkl, P.; Nagler, P.; Mornhinweg, J.; Schüller, C.; Korn, T.; Chernikov, A.; Huber, R. Direct Observation of Ultrafast Exciton Formation in a Monolayer of WSe_2. *Nano Lett.* **2017**, *17* (3), 1455−1460.
(39) Schmidt, P.; Vialla, F.; Latini, S.; Massicotte, M.; Tielrooij, K.-J.; Mastel, S.; Navickaite, G.; Danovich, M.; Ruiz-Tijerina, D. A.; Yelgel, C.; Fal'ko, V.; Thygesen, K. S.; Hillenbrand, R.; Koppens, F.

https://doi.org/10.1021/acs.nanolett.1c04741
Nano Lett. 2022, 22, 2561−2568

H. L. Nano-Imaging of Intersubband Transitions in van der Waals Quantum Wells. *Nat. Nanotechnol.* **2018**, *13* (11), 1035−1041.
(40) Hauer, B.; Engelhardt, A. P.; Taubner, T. Quasi-Analytical Model for Scattering Infrared Near-Field Microscopy on Layered Systems. *Opt. Express* **2012**, *20* (12), 13173−13188.
(41) Johnston, M. B.; Herz, L. M. Hybrid Perovskites for Photovoltaics: Charge-Carrier Recombination, Diffusion, and Radiative Efficiencies. *Acc. Chem. Res.* **2016**, *49* (1), 146−154.
(42) Lin, K.-Q.; Ong, C. S.; Bange, S.; Faria Junior, P. E.; Peng, B.; Ziegler, J. D.; Zipfel, J.; Bäuml, C.; Paradiso, N.; Watanabe, K.; Taniguchi, T.; Strunk, C.; Monserrat, B.; Fabian, J.; Chernikov, A.; Qiu, D. Y.; Louie, S. G.; Lupton, J. M. Narrow-Band High-Lying Excitons with Negative-Mass Electrons in Monolayer WSe_2. *Nat. Commun.* **2021**, *12* (1), 5500.
(43) Wang, G.; Marie, X.; Bouet, L.; Vidal, M.; Balocchi, A.; Amand, T.; Lagarde, D.; Urbaszek, B. Exciton Dynamics in WSe_2 Bilayers. *Appl. Phys. Lett.* **2014**, *105* (18), 182105.
(44) Lindlau, J.; Selig, M.; Neumann, A.; Colombier, L.; Förste, J.; Funk, V.; Förg, M.; Kim, J.; Berghäuser, G.; Taniguchi, T.; Watanabe, K.; Wang, F.; Malic, E.; Högele, A. The Role of Momentum-Dark Excitons in the Elementary Optical Response of Bilayer WSe_2. *Nat. Commun.* **2018**, *9* (1), 2586.
(45) Meckbach, L.; Stroucken, T.; Koch, S. W. Giant Excitation Induced Bandgap Renormalization in TMDC Monolayers. *Appl. Phys. Lett.* **2018**, *112* (6), 061104.
(46) Kira, M.; Koch, S. W. Many-Body Correlations and Excitonic Effects in Semiconductor Spectroscopy. *Prog. Quantum Electron.* **2006**, *30* (5), 155−296.
(47) Bai, Y.; Zhou, L.; Wang, J.; Wu, W.; McGilly, L. J.; Halbertal, D.; Lo, C. F. B.; Liu, F.; Ardelean, J.; Rivera, P.; Finney, N. R.; Yang, X. C.; Basov, D. N.; Yao, W.; Xu, X.; Hone, J.; Pasupathy, A. N.; Zhu, X. Y. Excitons in Strain-Induced One-Dimensional Moiré Potentials at Transition Metal Dichalcogenide Heterojunctions. *Nat. Mater.* **2020**, *19* (10), 1068−1073.
(48) Refaely-Abramson, S.; Qiu, D. Y.; Louie, S. G.; Neaton, J. B. Defect-Induced Modification of Low-Lying Excitons and Valley Selectivity in Monolayer Transition Metal Dichalcogenides. *Phys. Rev. Lett.* **2018**, *121*, 167402.
(49) Luo, L.; Chatzakis, I.; Patz, A.; Wang, J. Ultrafast Terahertz Probes of Interacting Dark Excitons in Chirality-Specific Semiconducting Single-Walled Carbon Nanotubes. *Phys. Rev. Lett.* **2015**, *114*, 107402.
(50) Zhou, Y.; Sung, J.; Brutschea, E.; Esterlis, I.; Wang, Y.; Scuri, G.; Gelly, R. J.; Heo, H.; Taniguchi, T.; Watanabe, K.; Zaránd, G.; Lukin, M. D.; Kim, P.; Demler, E.; Park, H. Bilayer Wigner Crystals in a Transition Metal Dichalcogenide Heterostructure. *Nature* **2021**, *595* (7865), 48−52.
(51) Wang, Z.; Rhodes, D. A.; Watanabe, K.; Taniguchi, T.; Hone, J. C.; Shan, J.; Mak, K. F. Evidence of High-Temperature Exciton Condensation in Two-Dimensional Atomic Double Layers. *Nature* **2019**, *574* (7776), 76−80.
(52) Wilson, N. P.; Lee, K.; Cenker, J.; Xie, K.; Dismukes, A. H.; Telford, E. J.; Fonseca, J.; Sivakumar, S.; Dean, C.; Cao, T.; Roy, X.; Xu, X.; Zhu, X. Interlayer Electronic Coupling on Demand in a 2D Magnetic Semiconductor. *Nat. Mater.* **2021**, *20* (12), 1657−1662.

https://doi.org/10.1021/acs.nanolett.1c04741
Nano Lett. 2022, 22, 2561−2568